# Development of high sensitivity oxide based strain gauges and pressure sensors

**K. Arshak · D. Morris · A. Arshak · O. Korostynska**

**Abstract** Strain gauges and pressure sensors are necessary tools for automotive, aerospace and biomedical monitoring applications. Of the various types of material, which can be used in their fabrication, oxides allow a degree of flexibility in their design. Furthermore, these devices are more rugged and cost effective than semiconductor sensors and have a higher sensitivity than metal-foil gauges. In this paper, the development of thin and thick film sensors based on oxides such as $V_2O_5$, $CeO_2$, $Bi_2O_3$, $In_2O_3$, $RuO_2$, $TiO_2$, MgO and $Nb_2O_5$ is discussed. The devices are evaluated in terms of their sensitivity or gauge factor, linearity, hysteresis and long term stability. Furthermore, different device configurations, planar and sandwich are compared. It is found that the devices presented in this work have sensitivity comparable to that of semiconductor gauges, with good long-term stability. This is particularly true of the sandwich devices. It is observed that oxide based strain gauges may offer an alternative to existing commercial gauges, for example, in applications involving load cells, torque wrenches and limb implants.

K. Arshak (✉) · O. Korostynska
Electronic and Computer Engineering Department, University of Limerick, Limerick, Ireland
e-mail: khalil.arshak@ul.ie

D. Morris · A. Arshak
Physics Department, University of Limerick, Limerick, Ireland

## 1 Introduction

Lord Kelvin first reported the relationship between electrical resistance and applied strain in wire conductors in 1856 [1]. However, it was not until the 1930's that commercial strain gauges came into effect. Their main purpose is to output a resistance, which changes in accordance with the strain experienced by the device. The difference in strain may be caused by the application of a compressive or tensile stress to the surface on which the sensor is attached. They are most commonly used in the automotive and aerospace industries, however, they have also found use in biomedical applications, for example, monitoring the performance of limb implants [2–4].

The most popular of types of strain gauges include metal foil, thin-film, semiconductor, and thick film. A comparison between the different technologies is shown in Table 1 [1, 5–7]. Strain sensitivity is one of the most important parameters to consider and is expressed as the gauge factor (GF), a dimensionless number describing the change in resistance as a ratio of applied strain. Sensitivity to temperature changes must also be quantified so that the correct gauge for the environmental condition can be chosen. The temperature coefficient of resistance (TCR) describes the parts per million change in resistance for every one degree change in temperature, while the temperature coefficient of gauge factor (TCGF) illustrates the change in sensitivity with temperature.

Table 1 illustrates that metal-foil gauges, while extremely stable, have a low sensitivity to strain and so cannot be used to make highly precise measurements. Alternatively, the fragile nature of the semiconductor gauges makes them impractical for use in a wide range

**Table 1** Properties of metal-foil, thin-film, semiconductor and thick-film strain gauges

| Strain gauge type | Description | GF | TCR (ppm/°C) | TCGF (ppm/°C) | Stability |
|---|---|---|---|---|---|
| Metal-foil | Consists of a metallic foil pattern, which is fabricated using an approach similar to that used in the production of printed circuit boards. The device is then bonded to the specimen of interest. The adhesive used and other installation techniques require careful choice, depending on the environmental conditions | 2–6 | 20 | 20–100 | Excellent |
| Thin-film | Can simply be described as a vacuum deposited thin film formed directly onto the surface of a strainable member. This removes the need for adhesives | 10–60 | 2000 | N/A | Good |
| Semiconductor | Fabrication involves slicing silicon crystals into thin sections, which are then mounted onto the specimen under test. These strain gauges are highly sensitive although they are difficult to install and operate due to their fragile nature | 50–200 | 400–2000 | 2000 | Good |
| Thick-film | Thick-film resistors are fabricated by screen-printing. This involves successive depositions and firing of specially formulated cermet or polymer pastes. A wide range of materials can be used, making the process extremely flexible. The performance of typical cermet pastes is shown in this table | 2–30 | 50–300 | 200–500 | Very good |

of monitoring application, despite their high sensitivity. Therefore it may be concluded that thin and thick film technologies must be relied upon for the cost effective production of high sensitivity, rugged sensors, which may be used in place of semiconductor devices.

The main advantage of thin and thick film technologies is their flexibility. A wide range of materials can be used to obtain a device with the required mechanical properties. This is particularly true for oxide based sensing layers, which have displayed high gauge factors and good long-term stability [8–15]. This paper reviews the use of a number of oxides, including vanadium oxide ($V_2O_5$), cerium oxide ($CeO_2$), bismuth oxide ($Bi_2O_3$), indium oxide ($In_2O_3$), ruthenium oxide ($RuO_2$), titanium oxide ($TiO_2$), magnesium oxide (MgO) and niobium pentoxide ($Nb_2O_5$), which have been employed in the fabrication of both thin and thick film strain gauges and pressure sensors. Each device is discussed in terms of composition, sensitivity, linearity, hysteresis and stability as defined in [8]. It can be seen that the production of highly sensitive devices can be achieved through the use of a single or combination of oxides.

# 2 Experimental procedure

## 2.1 Thin film

Corning 7059 borosilicate glass slides were used as substrates. These were prepared by boiling them in a 1% solution of Decon 90 detergent and deionised water for 10 min. They were then immersed in isopropanol slurry to remove final traces of grease and rinsed in deionised water for 5 min. Substrates were dried with compressed nitrogen gas in a class 1000 clean room environment. The final traces of microparticles were removed with ionic bombardment of the substrate at a pressure of 10 Pa (0.1 mbar) for 7–10 min.

The $Bi_2O_3/V_2O_5$ thin films were prepared by thermal evaporation, from tungsten boats, using an Edwards coating unit, with a nominal thickness of 100 nm, as measured by a crystal thickness monitor [12, 16]. Substrates were maintained at a temperature of 129°C ±2°C and the evaporation chamber was lined with aluminium foil to avoid contamination of and by the surrounding walls. The compositions evaporated were 10/90, 30/70, 40/60, 50/50, 60/30, 90/10 mol% of $Bi_2O_3$ to $Ve_2O_5$ and the final structure is shown in Fig. 1.

## 2.2 Thick film

In the preparation of thick film strain gauges and pressure sensors, alumina, stainless steel and polymer (Melinex®) substrates were used [8–10, 17]. All substrates were cleaned thoroughly prior to use. The devices were prepared by screen-printing, which involves forcing a viscous paste though a pre-patterned mesh onto the substrate below. The main advantages of this approach are high and precise line resolution,
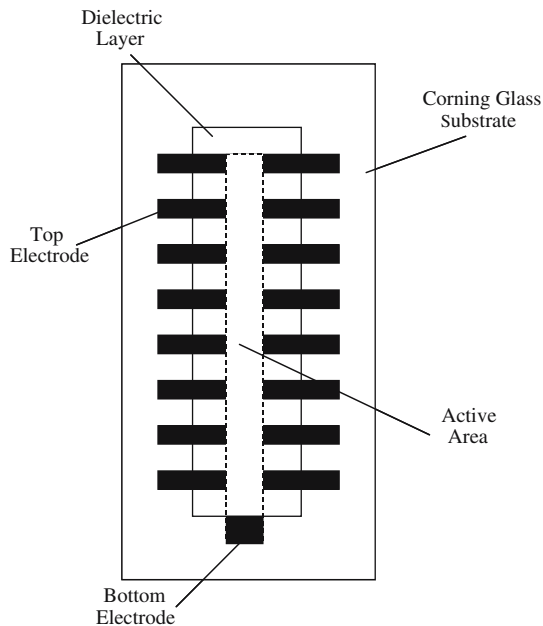
Fig. 1 Layout of thin film strain gauges

fast processing and economical use of paste [18]. Two structures were fabricated, firstly a planar strain gauge, which utilizes the piezoresistive effect and secondly a sandwich structure that can be either metal–resistor–metal (MRM) or metal–insulator–metal (MIM), as shown in Fig. 2.

Using a planar configuration, the mechanical properties of a commercial paste R8041 (supplied by Heraeus) were compared to two pastes, which were developed in house. The first composition, known as TFR1, contained 60% $Bi_2O_3$ and 40% $RuO_2$. The second, TFR2, consisted of 50% $Bi_2O_3$, 10% $In_2O_3$ and 40% $RuO_2$. Both TFR1 and TFR2 were combined with a lead bismuth borosilicate glass binder, ethyl cellulose (temporary binder) and the solvent terpinol-α. These pastes were chosen as their sheet resistance after firing is compatible (approximately 10 kΩ/Sq).
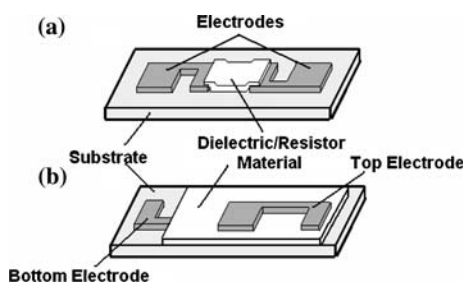


Fig. 2 Layout of (a) planar and (b) sandwich MRM and MIM devices

For stainless steel substrates, a glass adhesion dielectric layer of Heraeus IP211 was first deposited by screen-printing. Two layers of buffer dielectric, Heraeus IP9117S, were then printed. These act to insulate the strain gauge from the conductive substrate. A conductive layer of Heraeus C1214LS was then deposited to form the conductor terminals. Finally, the resistor layer (R8041, TFR1 or TFR2) was deposited. As these pastes are cermet or glass based, they were fired in a six zone belt furnace at a peak temperature of 850°C for 10 min with the total cycle time being 60 min.

For MRM devices the cermet pastes R8041, TFR1 and TFR2 were also used. In this case only sensors on stainless steel substrates were investigated. The device was insulated from the substrate surface as previously described. The bottom electrode was deposited first, followed by the conductive layer and finally the top electrode.

Strain gauges using an MIM configuration were prepared in a similar way to MRM devices. Alumina substrates were used in this case. Du Pont 4929 silver conductive paste was utilized for the electrodes, while $TiO_2$ was used to form the polymer paste for the dielectric layer. A polymer paste differs from a cermet paste in that the final film is not glassy in nature [19]. As oxides are usually used in the formation of cermet rather than polymer pastes, the powder was pre-fired by firstly mixing it with isopropanol to form a slurry, which was then wet ball milled in alcohol for 24 h. The alcohol was evaporated from this mixture by drying it at 120°C. The powder was then placed under a pressure of 2 tons to form a pellet, which was fired at 1250°C (at a rate 5°C per minute) in a vacuum of $6 \times 10^{-3}$ mbar for 5 h, followed by cooling (at a rate of 3°C per minute). After firing, the solid pellet was ground down to a powder using a Gy-RO Mill for 10 min. The powder was then mixed with 7 wt% of polyvinyl butyral (PVB), which was used as the binder. The solvent used to form the paste was ethylenglycol-monobutylether.

Another approach to the fabrication of thick film capacitors for strain and pressure sensing is the use of interdigitated electrodes [20]. The main advantage of this approach is one less process step during fabrication, when compared to sandwich capacitors, in addition to one-sided access to the sensing layer [21]. The mechanical properties of devices based on interdigitated electrodes were investigated for dielectric layers of $TiO_2$ (pre-fired and unfired), $CeO_2$, MgO and $Nb_2O_5$, which were unfired prior to use, on polymer substrates. In this study, electrodes with 25 fingers, of length 6 mm and width 0.2 mm was used. The spacing between the

electrodes was 0.2 mm. The thickness of the $TiO_2$, $CeO_2$, MgO and $Nb_2O_5$ layers were measured by profilometry and found to be 35.87, 22.5, 65.92 and 70μm, while their baseline capacitance was measured to be 7.5, 9, 6, and 8.9 pF, respectively.

## 2.3 Strain gauge test rig

In order to measure the change in resistance or capacitance with strain a specially designed test rig was constructed. Devices are placed in a cantilever beam arrangement, as shown in Fig. 3 and a load is applied at the free end [22]. This results in a deflection of the beam, which can be measured through the use of a linear variable differential transformer (LVDT) with a sensitivity of 0.7367 V/mm and a linearity of 0.3%. With knowledge of the beam displacement and geometry, the strain can be calculated in accordance with equation

$$\varepsilon = \frac{3xyh}{2L^3} \tag{1}$$

where $y$ is the displacement of the beam, $x$ is the distance from the centre of the device to the point where the load is applied, $h$ is thickness of the substrate and $L$ is the distance from where the substrate is clamped to the point where the load is applied.

## 2.4 Pressure sensor test rig

Pressure sensors were tested under hydrostatic pressure ranging from 0 to 17 kPa as this is typical of the range of pressures experienced within the human body. For example, pressures in the gastrointestinal tract typically vary between 6 and 16 kPa [20]. In order to achieve this a wireless interface, transmitter and rece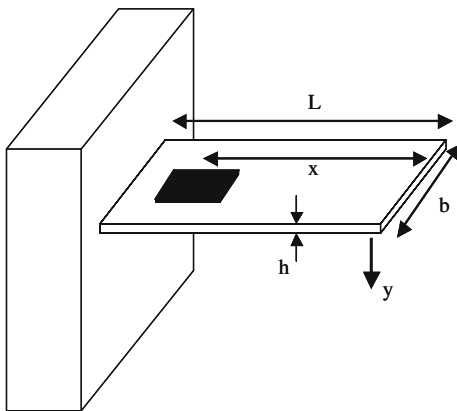iver circuit was designed. The sensor was protected from the liquid environment using a polymer membrane while the interface and transmitter was housed in a weatherproof box. The transmitter was placed outside the liquid environment and outputs a voltage corresponding to the sensor capacitance, according to Eq. (2)

$$C = \frac{1}{(V_o \times K_{VCO})(R_2 + 2R_1)\ln 2} \tag{2}$$

where, $V_o$ is the measured voltage from the Phase Locked Loop (PLL) unit, $K_{VCO}$ is the measured response of the Voltage Controlled Oscillator (VCO) (13.1 kHz/V) and $R_1$ and $R_2$ are the timer resistors. A block diagram of the interface, transmitter and receiver circuit is shown in Fig. 4.

## 3 Theoretical considerations

### 3.1 Sensor configuration and gauge factor

In this work, planar and sandwich strain gauges, based on the piezoresistive and piezocapacitive effect are investigated. The mechanisms governing the change in output with applied strain for both configurations are discussed in this section.

For a basic conductor, the resistance is known by examining the length, $l$, cross sectional area, $A$, and conductivity, $\sigma$ (or resistivity, $\rho$), as shown in Eq. (3) [11].
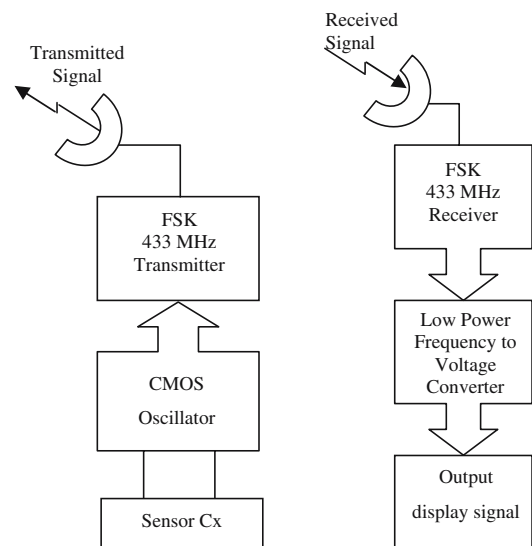


**Fig. 3** Cantilever beam arrangement



**Fig. 4** Block diagram of the interface, transmitter and receiver circuit used to make hydrostatic pressure measurements

$$R = \frac{l}{A\sigma} \qquad (3)$$

Longitudinal stress results in a fractional change in resistance $\delta R/R$, which can be attributed to changes in cross sectional area, length and conductivity as shown in Eq. (4).

$$\frac{\delta R}{R} = \frac{\delta \sigma}{\sigma} + \frac{\delta l}{l} + \frac{\delta A}{A} \qquad (4)$$

Thus in can be seen that it is a combination of geometrical and microstructural changes which cause the overall resistance alteration with applied strain [13]. Therefore, the geometrical changes can be grouped using Poissons ratio ($v$) so that Eq. (5) results.

$$\frac{\delta R/R}{\delta l/l} = (1 + 2v) - \frac{\delta \sigma/\sigma}{\delta l/l} = GF \qquad (5)$$

It is generally accepted that changes in the geometrical factors alone will result in a GF of 2 [13, 14]. As typical GF's for thin and thick film devices may lie anywhere between 2 and 60 (sometimes higher), it can be seen that the piezoresistive or $\delta\sigma/\sigma$ effect, linked to changes in microstructure, dominates.

In calculating the gauge factor for piezoresistive strain gauges, a simplified version of Eq. (5) is used, where $R$ is the resistance and $\varepsilon$ is the applied strain. This relationship is shown in Eq. (6).

$$GF = \frac{\Delta R/R}{\varepsilon} \qquad (6)$$

It is important to note that Eq. (6) refers to the longitudinal gauge factor. However, if the orientation of the strain gauge is changed by 90°, the gauge will experience transverse strain and so a second gauge factor would result [10]. The relationship between longitudinal ($GF_L$) and transverse ($GF_T$) gauge factors is shown in Eq. (7).

$$GF_L - GF_T = 2(1 + v) \qquad (7)$$

Taking thick film resistors as an example, Poissons ratio ($v$) has been found to be approximately 0.22. Therefore, the theoretical difference between the two gauge factors is 2.44, with $GF_L$ being the higher of the two. At all stages in this work, it is the longitudinal gauge factor, which is measured.

In the case of sandwich capacitors, based on the piezocapacitive effect, the capacitance, $C$, can be calculated if the permittivity of free space, $\varepsilon_o$, the permittivity of the dielectric, $\varepsilon_r$, the area of the capacitor plates, $A$ and the distance between them, $d$, are known. This is illustrated in Eq. (8).

$$C = \frac{\varepsilon_o \varepsilon_r A}{d} \qquad (8)$$

As in the case of piezoresistive gauges, the applied strain results in geometrical and structural changes, shown in Eq. (9),

$$\frac{\delta C}{C} = \frac{\delta k}{k} + \frac{\delta A}{A} - \frac{\delta h}{h} \qquad (9)$$

where, $\delta k/k$ represents the change in the materials dielectric properties, while $\delta A/A$ and $\delta h/h$ represents variations in the area of the electrodes and the dielectric thickness, respectively. Grouping the geometrical and structural changes through the use of the Poissons ratio leads to an expression of the devices GF given in Eq. (10) [8].

$$GF = \frac{\Delta C/C}{\varepsilon} \qquad (10)$$

For interdigitated capacitors, the baseline capacitance is determined by the electrode gap ($G$), finger width ($W$), finger length ($L$), spatial wavelength ($\lambda = 2[W+G]$) and the metallization ratio ($\eta = 2W/\lambda$) [23]. As these parameters are fixed, any change in capacitance under strain or pressure is due to deformation of the dielectric material as described in [8, 24]. So it can be seen that for this device, polymer pastes are preferred as they are more compliant.

## 4 Results and discussion

### 4.1 Thin film strain gauges

One of the strongest advantages of thin film strain gauges over other devices is that they can be directly bonded to the strainable member, making it particularly useful when dealing with unusual surfaces, for example a torque wrench or limb implant. Oxide materials are known to posses strong piezoresistive properties, which may be used in the production of strain gauges [25]. For example, vandate based oxides (eg. $V_2O_5$) have been shown to exhibit significant piezoelectric properties and may be a useful alternative to existing strain gauges [11]. However, the variable valency of the vanadium ion gives rise to instabilities [26]. As a result, a second material is required to provide stability without reducing sensitivity. Previous investigations into the use of a $V_2O_5$–$CeO_2$

composition have shown that while the addition of $CeO_2$ has been successful in creating stability, it adversely affects the materials gauge factor [11]. As a result bismuth oxide $Bi_2O_3$ was used, due to its piezoresistive properties [16].

The initial molar ratios of the mixed oxide, $V_2O_5$–$Bi_2O_3$, were varied and the effect on strain sensitivity investigated. The results are shown in Fig. 5, where it can be seen that the gauge factor varied between 4 and 16. There is little correlation between the initial molar percentage of $Bi_2O_3$ and the gauge factor. Each composite was examined over a period of 1 month. The film with an initial composition of 40 mol% $Bi_2O_3$:60 mol% $V_2O_5$ was observed to become electrically unstable, with more than a 100% change in resistance occurring over a 3 week period, while the composition consisting of 90 mol% $Bi_2O_3$:10 mol% $V_2O_5$ changed by only 2% over a month, as shown in Fig. 6. Therefore, their temporal stability improved as the molar percentage of $Bi_2O_3$ was increased. This is attributed to the fact that $Bi_2O_3$ is less prone to oxidation than $V_2O_5$ [16].
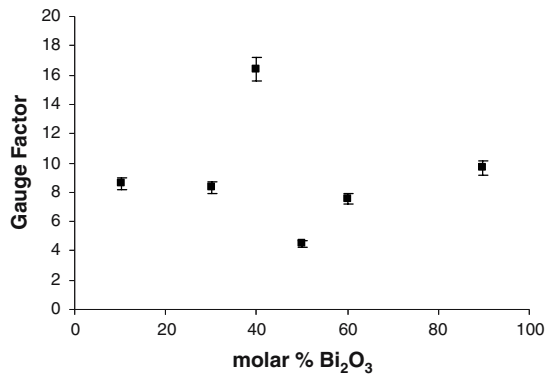
A study of the sensitivity of gauges produced under various deposition conditions was conducted in order to determine the parameters, which have the highest effect on sensitivity. The rate of evaporation on a number of films with a high molar percentage of $Bi_2O_3$ was varied. In general, the sheet resistance was found to decrease when the rate of evaporation increased. The effect of sheet resistance on the gauge factor is shown in Fig. 7. It can be seen that the maximum sensitivity corresponds to the highest sheet resistance. However, the variation in results suggests that other parameters are important in determining the final response of the strain gauge.

It is thought that the decrease in resistance with increased evaporation rates and the subsequent changes in gauge factor are due to the phase separation of the $Bi_2O_3$. Therefore, a reactive evaporation of the composite at different oxygen pressures was investigated in an attempt to control the phase separation of $Bi_2O_3$ and study its effects on the gauge factor. The results are shown in Fig. 8, where it can be seen that a strong relationship has resulted, with the gauge factor



Fig. 5 Gauge factor as a percentage of molar percentage $Bi_2O_3$ into $V_2O_5$



Fig. 7 Dependence of gauge factor on the sheet resistance of films

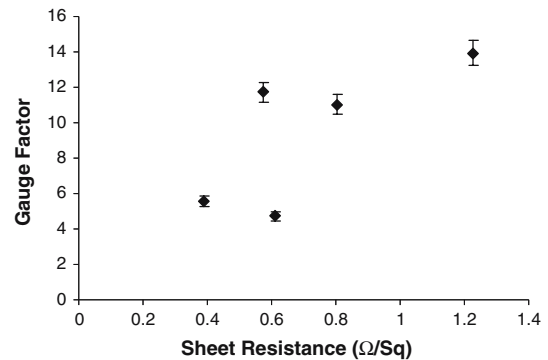

Fig. 6 Gauge resistance verses time for thin films containing 40, 50, 60 and 90% of $Bi_2O_3$ into $V_2O_5$
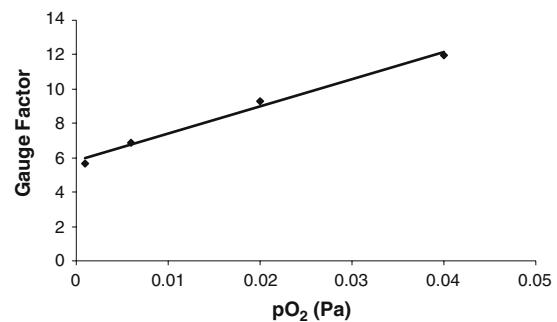


Fig. 8 Dependence of gauge factor on oxygen pressure during evaporation for thin films with an initial composition of 90 mol% $Bi_2O_3$:10 mol% $V_2O_5$

increasing linearly up to a value of 9.2 for a pressure of 0.02 Pa ($2 \times 10^{-4}$ mbar) $O_2$. From the experiments described above, the final composition and deposition parameters chosen for this device was a 90 mol% $Bi_2O_3$:10 mol% $V_2O_5$ evaporated at an oxygen pressure of 0.006 Pa ($6 \times 10^{-5}$ mbar).

The temporal stability of this composition, over a period of 1 month, was compared to that of compositions containing 40, 50, 60 and 70% $Bi_2O_3$. The results are shown in Fig. 9, where it can be seen that for lower molar percentages of $Bi_2O_3$ there are significant changes. Gauges with 40 and 50% $Bi_2O_3$ became electrically unstable after 3 weeks, while the gauge factor of the sample with 90% $Bi_2O_3$ was observed to remain stable over the time period, as previously observed. A full investigation of the optical and electronic properties of $V_2O_5$–$Bi_2O_3$ thin films has been conducted, the results are given in [12].

### 4.2 Thick film strain gauges

#### 4.2.1 Planar and sandwich piezoreistsive strain gauges

Holmes first discovered the piezoresistive properties of thick-film resistors in the early 1970's [27]. Since then there has been a considerable amount of research undertaken in order to improve the response of the sensing elements [17]. One of the main advantages of thick film devices is their rugged nature, making them suitable for use in harsh environmental and medical conditions.

The most commonly used pastes in the fabrication of thick film strain gauges are based on ruthenium. Examples include ruthenium dioxide ($RuO_2$), which has a rutile structure and ruthenium trioxides, which have a pyrochlore structure [28]. However, it is expensive, thus increasing the final cost of the gauge.
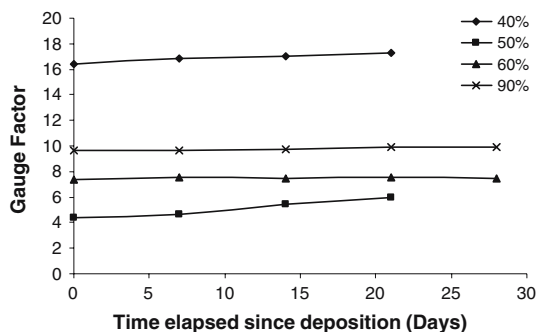
In this work, the properties of three pastes were evaluated in both a planar and sandwich arrangement. The commercial paste R8041 is based on $RuO_2$, while the pastes developed in house were known as TFR1 and TFR2 have compositions of 60% $Bi_2O_3$/40% $RuO_2$ and 50% $Bi_2O_3$/10% $In_2O_3$/40% $RuO_2$, respectively. This investigation was undertaken in order to assess (i) the sensitivity of pastes with reduced ruthenium content and (ii) the effectiveness of each structure.

For planar resistors, the use of two substrates was investigated, 96% alumina and stainless steal. A plot of the fractional change in resistance with strain for each composition printed on stainless steel and alumina can be seen in Fig. 10. It is important to note that alumina substrates cannot withstand large strains, due to their brittle nature and therefore have been tested in the range 0–500μstrain, while devices on stainless steel substrates have been tested up to 2500μstrain.

It can be seen from Table 2 that the TFR's printed and fired on insulated stainless steel show good characteristics over the entire range. They also showed a higher level of sensitivity, which may be due to an improved adhesion, achieved through the fired
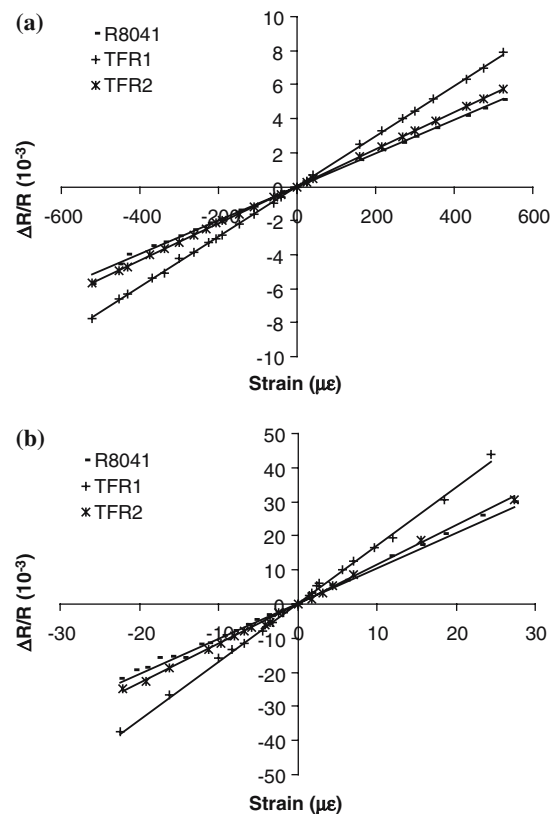


Fig. 9 Gauge factor verses time for thin films containing 40, 50, 60 and 90% of $Bi_2O_3$ into $V_2O_5$



Fig. 10 Response and linearity, as measured for planar cermet gauges on (a) 96% alumina and (b) stainless steel

**Table 2** Gauge factor, % linearity and % hystersis recorded for strain gauges fabricated using R8041, TFR1 and TFR2
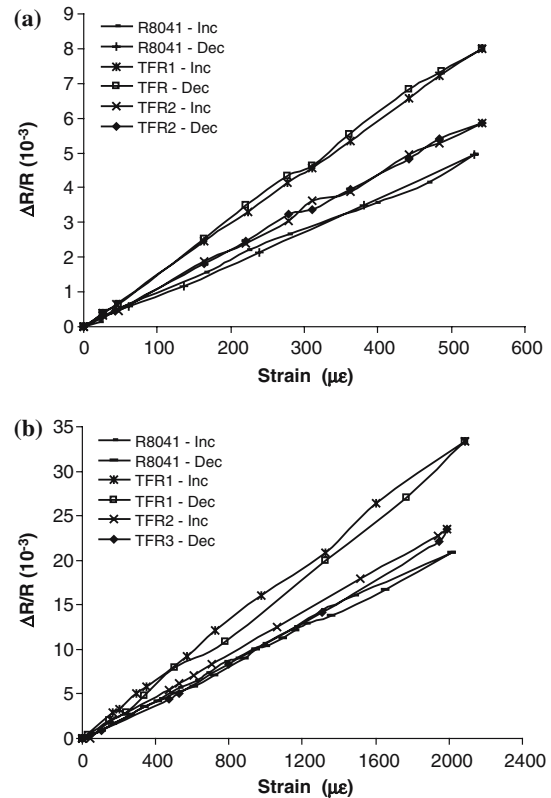
|       |        |           | GF   | % Linearity | % Hysteresis |
|-------|--------|-----------|------|-------------|--------------|
| R8041 | Planar | SS        | 11   | 2           | 4            |
|       |        | Alumina   | 10   | 2.5         | 3            |
|       | MRM    | Resistive | 87   | 2.7         | 9.3          |
|       |        | Capacitive| 77   | 0.4         | 2.4          |
| TFR1  | Planar | SS        | 17   | 3           | 7            |
|       |        | Alumina   | 15   | 3           | 6            |
|       | MRM    | Resistive | 94   | 4.7         | 9            |
|       |        | Capacitive| 82   | 0.8         | 3.2          |
| TFR2  | Planar | SS        | 11   | 1.5         | 7.5          |
|       |        | Alumina   | 11   | 2           | 5            |
|       | MRM    | Resistive | 67   | 4.3         | 10           |
|       |        | Capacitive| 77.5 | 0.8         | 2.5          |

dielectric layers [22]. It is also important to note the higher sensitivity of TFR1 when compared to R8041 and TFR2. This is in agreement with the results displayed for thin film compositions of $Bi_2O_3$–$V_2O_5$, where increasing the percentage of bismuth oxide present, improved the sensitivity. Furthermore, the addition of a stability modifier such as $In_2O_3$ has resulted in a decreased strain sensitivity, similar to the effect of $CeO_2$ on $V_2O_5$ [11].

Examining the linearity of each gauge shows that there is little variation in results. However, the measured hysteresis is quite high and is thought to be due to a number of factors, including poor milling and blending of the pastes, the existence of large particles (> 2μm) within the fired structure and inaccuracy of the test rig system due to movement of the LVDT under the large applied strains. Another possibility is the presence of microcracks in the films which become significant at higher strain levels [19]. The hysteresis for devices on stainless steel and alumina substrates is shown in Fig. 11.

The MRM gauge configuration has some significant advantages over its planar counterpart. In this study, the change in both resistance and capacitance with strain was recorded. The results are shown in Fig. 12, where the first and most notable of these advantages is an ≈ 800% increase in strain sensitivity. This can be explained by considering the high ratio of geometric to piezoresistive properties present in the planar gauge structure, which results in a relatively low sensitivity [29]. However, this is not true for a MRM configuration. The increase in effective contact area and reduction in thickness causes a decreased geometric effect and an increase in piezoresistivity.

In addition to high sensitivity, the MRM gauges must show acceptable levels of linearity and hysteresis if they are to be used in commercial applications.



**Fig. 11** Hysteresis, measured for planar cermet gauges on (**a**) 96% alumina and (**b**) stainless steel

There is a slight increase in linearity of the MRM gauges when compared to the planar devices. However, this could be attributed the large increase in sensitivity [8]. The linearity of the capacitive form of this gauge is significantly lower that than recorded for the resistive. This can be attributed to geometrical effects, with the structure being more dependent on the effective contact area, than the distance between electrodes.

An increase in the measured values of hysteresis for the resistive MRM gauges has been recorded and is compatible with its linearity, as shown in Fig. 13. In addition, the capacitive form of the MRM gauges shows a lower hysteresis, which can also be attributed to the reduced linearity error.

### 4.2.2 Capacitive strain gauges

The development of capacitive strain gauges began in the 1960's and was driven by the need for a device based only on geometrical changes, i.e. alterations in the electrode area or the thickness between them [1]. This relied on the presence of moving parts within the gauge, which can lead to packaging and reliability constraints.
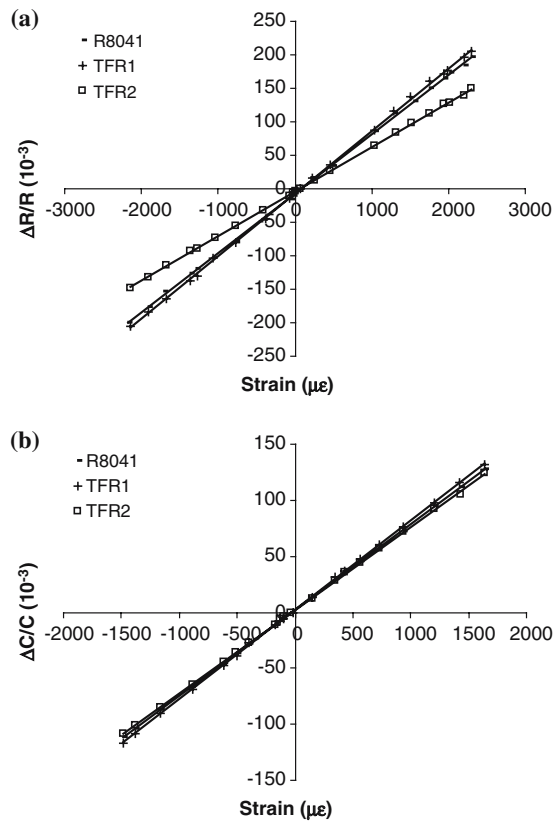
**(a)**



**(b)**



**Fig. 12** Shows the response and linearity, as measured for (**a**) resistive and (**b**) capacitive forms of the MRM device

**(a)**



**(b)**



**Fig. 13** Hystersis, as measured for (**a**) the resistive and (**b**) the capacitive form of the MRM device

In this section, a physical capacitor is presented, which utilized both changes in geometry and in the dielectric material. Polymer pastes are preferred for this application as the cermet pastes used in the production of planar and MRM gauges require long firing cycles and are also conductive in nature. However, it is sufficient to cure polymer thick film devices in an oven at 150–200°C and the sensitivity can be comparable to cermet devices [14, 30, 31].

The polymer paste was based on titanium dioxide ($TiO_2$), as it is cost effective and chemically stable [32]. The devices were fabricated on alumina substrates using two configurations; a planar capacitor formed using interdigitated electrodes and a sandwich device similar to the MRM gauges. The results are shown in Table 3. The sandwich structure was considerably more sensitive, with a gauge factor of 30 recorded. It is thought that the difference in gauge factor is due to the design of the interdigitated structures as the sensor capacitance is more dependent on the position of the electrodes, than the thickness of the dielectric layer above it [8, 23]. The difference in linearity can be attributed to the sensitivity of each device, as shown in the case of the cermet pastes R8041, TFR1 and TFR2.
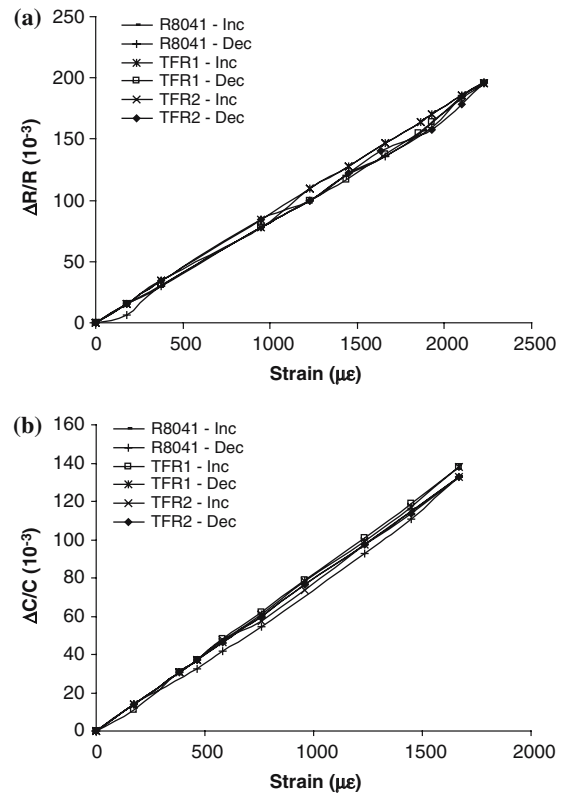
The sensitivity and linearity of the interdigitated and sandwich design can be seen in Fig. 14.

It can also be seen, from Fig. 15 that there is an order of magnitude difference in the hysteresis for the planar and sandwich structures, which can also be attributed to differences in the recorded sensitivity and linearity. From these results it can be concluded that a highly insulative, capactive strain gauge could be used as an alternative to MRM gauges, which are conductive in nature. Capacitive gauges are useful in applications where a low power consumption is required [33]. This is particularly the case in the area of biomedical monitoring, where a device is implanted in the body for a period of time and readings are sent wirelessly to an external receiver.

**Table 3** Shows the gauge factor, linearity and hysteresis recorded for interdigitated and sandwich capacitors

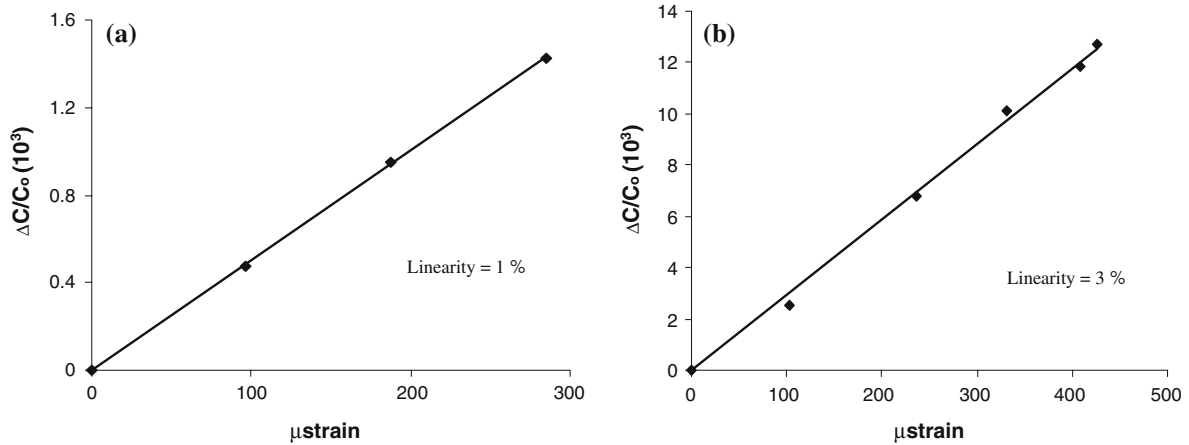|                     | GF  | % Linearity | % Hysteresis |
| ------------------- | --- | ----------- | ------------ |
| Interdigitated      | 5   | 1           | 0.7          |
| Sandwich (MIM)      | 30  | 3           | 7            |

**Fig. 14** Response and linearity, as measured for (**a**) an interdigitated capacitor and (**b**) a sandwich capacitor
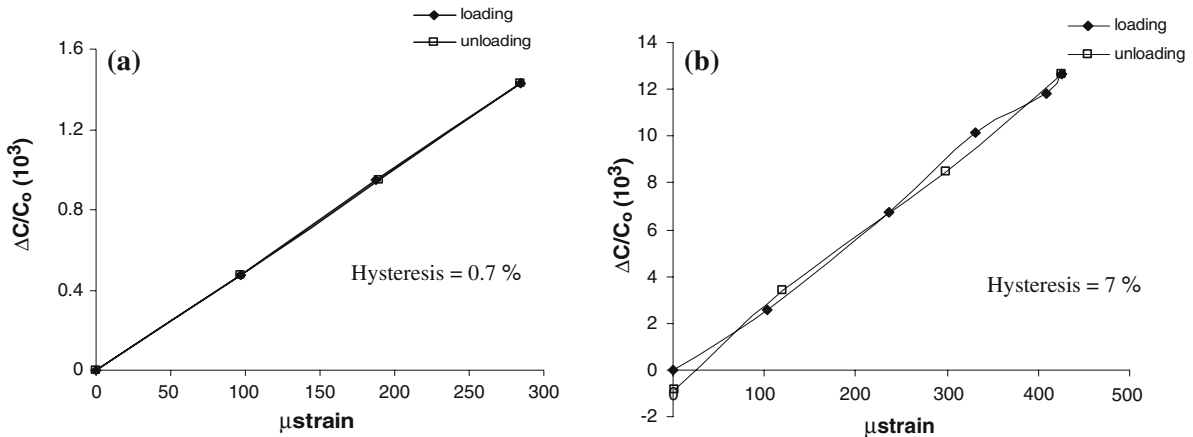


**Fig. 15** Hysteresis, as measured for (**a**) an interdigitated capacitor and (**b**) a sandwich capacitor

### 4.3 Thick film pressure sensor

Thick film capacitors are also finding use in pressure sensing applications as an alternative to the traditional devices, which are based on the movement of an electrode relative to a fixed reference [34]. In a thick film capacitor, there are no moving parts and therefore many reliability and packaging issues can be avoided. One particular area where such devices could find use is wireless monitoring of pressure changes in the human body, for research in areas such as cardiology and gastroenterology [35]. In this section, a brief overview of the performance of oxide pressure sensors based on interdigitated electrodes is presented.

Four oxides are investigated and compared. These are $CeO_2$, $TiO_2$, $MgO$ and $Nb_2O_5$, which have not been fired prior to screen-printing. These oxides were chosen as they posses a low toxicity and are easily avail-

able. Each capacitor was tested under hydrostatic pressure in the range 0–17 kPa.

The response of each composite is shown in Fig. 16 and was measured to be 24.4, 45.5, 26.6 and 65.9 mV for $CeO_2$, $TiO_2$, $MgO$ and $Nb_2O_5$, respectively. It can be seen that the highest sensitivity to pressure changes are observed for oxides with the smallest particle size. For both $TiO_2$ and $Nb_2O_5$, the particle size is in the order of a few hundred nanometres, which for $Ce_2O_3$ and $MgO$ it is a couple of microns. The non-linear output can in part be attributed to the use of a phase locked loop in the circuitry. This was done to minimize power consumption.

The hysteresis of each device was measured, as shown in Fig. 17. It was found that $Nb_2O_5$ displayed the highest degree of hysteresis at 8%, while $TiO_2$ was the most stable at 3.8%. Both $CeO_2$ and $MgO$ displayed a hysteresis of 7%. This is generally attributed
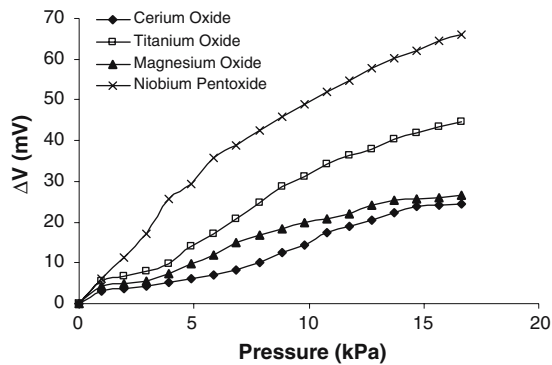
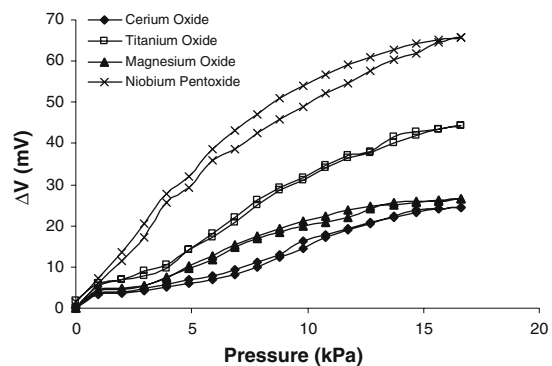**Fig. 16** Response recorded for interdigitated capacitors formed



**Fig. 17** Hysteresis, recorded for interdigitated capacitors formed with, $CeO_2$, $TiO_2$, MgO and $Nb_2O_5$

to friction and structural changes within the material [36].

## 5 Conclusions

In this work, the performance of both thin and thick film strain gauges and pressure sensors have been evaluated, as a high sensitivity and reliable alternative to existing devices. It was found that the performance of thin film sensors depends on both the composition and deposition parameters used during fabrication. Furthermore, as was observed for thick film devices, sandwich structures offer a superior sensitivity to planar devices. However, the composition of the sensing layer was also of high importance in determining the final characteristics of the strain gauge. Finally, an investigation into the properties of thick film pressure sensors showed that by changing the composition of the sensing layer, the output of the device could be altered. It can be concluded, from the results presented in this work that oxide based sensors have a wide range of flexibility, are highly reliable and can be used in a

wide range of monitoring applications, for example torque wrenches, limb implants and other medical situations where pressure needs to be observed in the long term.

## References

1. A.L. Window, G.S. Holister, *Strain Gauge Technology* (Elsevier Applied Science, London New York, 1982)
2. N.M. White, J.D. Turner, Meas. Sci. Technol. **8**, 1 (1997)
3. A. Huge, M.E. Kreis et al., J. Surg. Res. **74**, 112 (1998)
4. J. Guo, H. Kuo et al., in *Proceedings of the Solid State Sensor, Actuator and Microsystems Workshop*, South Carolina, 2004
5. R.S. Figliola, D.E. Beasley, *Theory and Design for Mechanical Measurements* (Wiley, Chichester New York, 2000)
6. F. Ansari, *Design and Modeling of Thick-Film Strain Gauge Transducer* (University of Limerick, 1994)
7. S. Chitale, C. Huang et al., *Hybrid Circuit Technology* (1989) p. 45
8. A. Arshak, K. Arshak et al., Sensor. Actuat. A-Phys. **122**, 242 (2005)
9. D.G. Collins, K.I. Arshak, Microelectr. J. **27**, 59 (1996)
10. K.I. Arshak, D. Collins et al., Mater. Design **15**, 149 (1994)
11. K.I. Arshak, G.A. Landers et al., Int. J. Electron. **76**, 1011 (1994)
12. K.I. Arshak, R.L. Perrem, J. Phys. D. Appl. Phys. **26**, 1098 (1993)
13. M. Hrovat, D. Belavic et al., Sensor. Actuat. A-Phys. **107**, 261 (2003)
14. M. Hrovat, D. Belavic et al., J. Eur. Ceram. Soc. **23**, 1441 (2003)
15. D. Belavic, M. Pavlin et al., in *Proceedings of the IMAPS*, Poland, 2000
16. K. Arshak, R. Perrem, Sensor. Actuat. A-Phys. **36**, 73 (1993)
17. K.I. Arshak, F. Ansari et al., Meas. Sci. Technol. **8**, 58 (1997)
18. H. Altenburg, J. Plewa et al., Pure. Appl. Chem. **74**, 2083 (2002)
19. C.A. Harper, in *Handbook of Thick Film Hybrid Microelectronics: A Practical Sourcebook for Designers, Fabricators and Users* (McGraw-Hill Book Company, New York, 1974)
20. A. Arshak, K.I. Arshak et al., *Proceedings of the MRS Spring Meeting*, San Francisco, (edited by M. S. Shur, P. Wilson, et al. City, 2005)
21. A.V. Mamishev, K. Sundara-Rajan et al., P. IEEE **92**, 808 (2004)
22. K.I. Arshak, F. Ansari et al., Int. J. Electron. **76**, 365 (1994)
23. R. Igreja, C.J. Dias, Sensor Actuat. A-Phys. **112**, 291 (2004)
24. T.R. Filanc-Bowen, G.H. Kim et al., P. IEEE **2**, 1648 (2002)
25. R.L. Perrem, in *Thin Film Strain Gauge: An Investigation into the Properties of the Mixed Oxide* $V_2O_5$–$Bi_2O_3$ (University of Limerick, 1993)
26. N.F. Mott, J. Non-Cryst. Solids **1**, 1 (1968)
27. P.J. Holmes, Microelectron. Reliab. **12**, 395 (1973)

28. J.J. Licari, L.R. Enlow, in *Hybrid Microcircuit Technology Handbook: Materials, Processes, Design, Testing and Production* (Noyes Publications, Park Ridge, 1988)
29. A. Cattaneo, R. Dell'Acqua et al., IEEE T. Compon. Hybr. (1980)
30. T.V. Papakostas, N.M. White, J. Phys. D. Appl. Phys. **33**, L73 (2000)
31. K.I. Arshak, D. Collins et al., Int. J. Electron. **77**, 387 (1994)
32. D.M. Brunette, in *Titanium in Medicine: Material Science, Surface Science, Engineering, Biological Responses and Medical Applications* (Springer, London, 2001)
33. R. Puers, Sensor Actuat. A-Phys. **37–38** (1993) 93
34. D. Crescini, V. Ferrari et al., Meas. Sci. Technol. **8**, 71 (1997)
35. C. Yang, C. Zhao et al., Biosens. Bioelectron. **19**, 51 (2003)
36. J. Fraden, in *Handbook of Modern Sensors: Physics, Designs, and Applications* (Springer-Verlag, New York, 1996)